and is slightly tapered as it merges with the adsorbed film. However, in employing this method, attention must be paid to the discontinuity in the interfacial curvature, which can be made negligible by properly selecting the matching point between an interline and thin film solutions.

References

deGennes, P. G., 1985, "Wetting: Statics and Dynamics," *Rev. Mod. Phys.*, Vol. 57, pp. 827–861.

Dussan, E. B., V, Rame, E., and Garoff, S., 1991, "On Identifying the Appropriate Boundary Conditions at a Moving Contact Line: An Experimental Investigation," *J. Fluid Mech.*, Vol. 230, pp. 97–116.

Israelachvili, J. N., 1989, *Intermolecular and Surface Forces*, Academic Press, New York.

Stephan, P. C., and Busse, C. A., 1990, "Theoretical Study of an Evaporating Meniscus in a Triangular Groove," presented at the 7th Int. Heat Pipe Conf., Minsk, USSR.

Swanson, L. W., and Herdt, G. C., 1992, "Model of the Evaporating Meniscus in a Capillary Tube," ASME JOURNAL OF HEAT TRANSFER, Vol. 114, pp. 434–441.

Wayner, P. C., Jr., Kao, Y. K., and Lacroix, L. V., 1976, "The Interline Heat Transfer Coefficient of an Evaporating Wetting Film," *Int. J. Heat Mass Transfer*, Vol. 19, pp. 487–492.

Wayner, P. C., Jr., and Schonberg, J. F., 1990, "Heat Transfer and Fluid Flow in an Evaporating Extended Meniscus," presented at the 9th International Heat Transfer Conference, Israel.

Wayner, P. C., Jr., DasGupta, S., and Schonberg, J. F., 1991, "Effect of Interfacial Forces on Evaporative Heat Transfer in a Meniscus," WL-TR-91-2061.

Welter, D., 1991, "The Effect of Evaporation on the Dynamic Capillary Pressure in Heat Pipes," M.S.M.E. Thesis, University of Dayton.

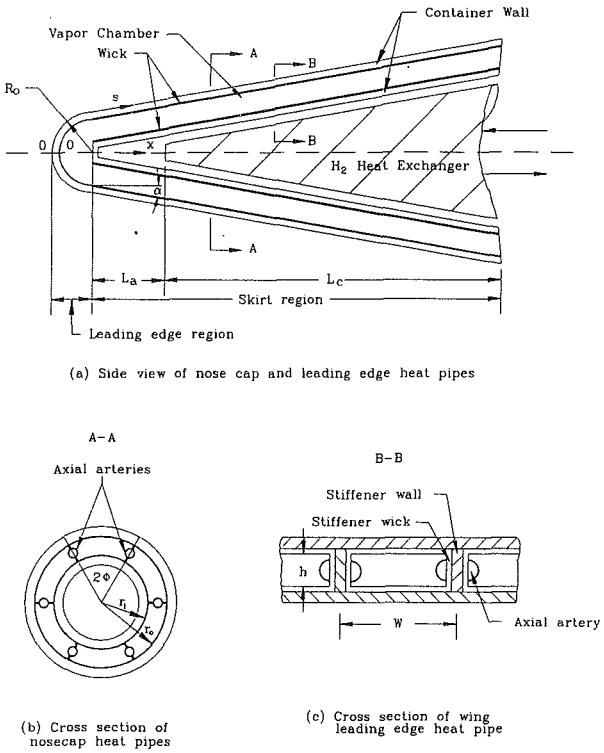

Fig. 1 Configuration of nosecap and wing leading edge heat pipes

Conjugate Modeling of High-Temperature Nosecap and Wing Leading Edge Heat Pipes

Y. Cao[1] and A. Faghri[1]

Introduction

Future hypersonic vehicles will be subjected to intense aerodynamic heating at the nosecap and wing leading edges. Three methods (barrier coatings, internal active cooling, and high-temperature heat pipes) have been proposed for cooling these hypersonic aircraft structures.

It appears that heat pipes are one of the most promising choices for cooling hypersonic vehicle structures due to their efficiency and reusability (Camarda, 1988). A typical nosecap heat pipe and a wing leading edge heat pipe with back wall radiation to a hydrogen coolant sink are schematically shown in Fig. 1. The nosecap heat pipe design consists of a conical annular vapor space between two shells, whereas the vapor space of the leading edge heat pipe has a rectangular cross section. In addition to the radiation heat transfer from the outer wall to space, the inner wall will transfer heat to the hydrogen-cooled tube heat exchanger by radiation.

In this paper, a generalized finite-difference computational methodology is presented to model the transient and steady-state behavior of the nosecap and the leading edge heat pipes developed by the U.S. Air Force for the National Aerospace Plane (NASP). The numerical simulation includes a consideration of capillary and sonic limits in the wick structures.

Mathematical Formulation

Heat Pipe Walls and Wicks. In this paper, a body-conforming coordinate system with a multiblock approach (Cao and Faghri, 1991) was used for the heat pipe walls and wicks. The energy equation in vectorial form is

$$(c\rho)\frac{\partial T}{\partial t} = \nabla \cdot k \nabla T \tag{1}$$

where

$$k = \begin{cases} k_w \\ k_{\text{eff}} \end{cases} \quad (c\rho) = \begin{cases} c_w \rho_w & \text{for the wall} \\ \omega (c\rho)_l - (1-\omega)(c\rho)_{wm} & \text{for the wick} \end{cases} \tag{2}$$

The effective thermal conductivity of the wick is k_{eff}, and ω is the wick porosity. In the nose region of the nosecap heat pipe, a spherical coordinate system is used; in the leading edge region of the wing leading edge heat pipe, a cylindrical coordinate system is applied. In the skirt regions of the nosecap and wing leading edge heat pipes, a cylindrical coordinate system and a Cartesian system are employed, respectively.

In the above formulation, the wick structures were assumed to be isotropic and homogeneous. Also, the effect of liquid flow through the wick on the temperature distribution in the wick structure was neglected. For the nosecap heat pipe, only the part with apex angle of 2ϕ shown in Fig. 1 needs to be modeled due to the symmetric geometry. For the wing leading edge heat pipe, the heat distributions near the stagnation line are nearly symmetric, and the heat pipe was divided in the spanwise direction into a number of vapor channels with width

[1]Department of Mechanical and Materials Engineering, Wright State University, Dayton, OH 45435.

Contributed by the Heat Transfer Division and presented at the ASME Winter Annual Meeting, Anaheim, California, November 8–13, 1992. Manuscript received by the Heat Transfer Division September 1992; revision received February 1993. Keywords: Conjugate Heat Transfer, Heat Pipes and Thermosyphons, Numerical Methods. Technical Editor: R. Viskanta.

W by the stiffener walls. Therefore, a typical vapor chamber of width W was modeled with symmetric boundary conditions applied on the stiffener walls and the stagnation line.

Vapor Flow. For the vapor flow in the heat pipe, the transient compressible quasi-one-dimensional vapor flow model of Cao and Faghri (1991) is adopted. The conservation of mass and momentum equations are:

$$\frac{\partial}{\partial t}(\rho A)+\frac{\partial}{\partial x}(\rho UA)=v\rho\frac{dS}{dx} \tag{3}$$

$$\frac{\partial}{\partial t}(A\rho U)+\frac{\partial}{\partial x}(A\rho U^2)=-\frac{\partial}{\partial x}\left[A\left(p-\frac{4}{3}\mu\frac{\partial U}{\partial x}\right)\right]-\frac{1}{2}f\rho U^2\frac{dS}{dx}\cos\alpha+\rho v^2\frac{dS}{dx}\sin\alpha \tag{4}$$

where A is the cross-sectional area of the vapor channel, U is the average axial vapor velocity, S is the channel wall surface area between the leading edge and position x, f is the friction coefficient, α is the local slope of the heat pipe wall, and v is the radial vapor injection or suction velocity. The perfect gas law is employed to account for the compressibility of the vapor:

$$p=\rho RT_v \tag{5}$$

where R is the gas constant. The vapor temperature and pressure are related by the Clausius–Clapeyron equation:

$$\frac{dp}{p}=\frac{h_{fg}}{R}\frac{dT_v}{T_v^2} \tag{6}$$

The vapor flow can be considered to be laminar along the heat pipe length due to the relatively small axial Reynolds number (Cao and Faghri, 1990; Faghri et al., 1991). The friction coefficients are functions of the cross-sectional geometry of the vapor chambers, and are given by Shah and Bhatti (1987). In the nose region of the nosecap heat pipe, the modeled vapor chamber is a circular sector with apex angle 2ϕ. The friction coefficient in this region is

$$f\,\mathrm{Re}_h=12(1+0.5059\,\phi-0.3948\,\phi^2+0.1875\,\phi^3-0.0385\,\phi^4)\quad(0\le 2\phi\le\pi) \tag{7}$$

In the skirt region of the nosecap heat pipe, the modeled vapor chamber is an annular sector with apex angle 2ϕ. The friction coefficient for this case is

$$f\,\mathrm{Re}_h=24\left\{\left[1-\frac{0.63}{\phi}\left(\frac{1-r^*}{1+r^*}\right)\right]\left[1+\frac{1}{\phi}\left(\frac{1-r^*}{1+r^*}\right)\right]^2\right\}^{-1} \tag{8}$$

where $r^*=r_i/r_o$, and r_i and r_o are the inner and outer radii of the annular sector. This equation is applicable for $\phi>\phi_{\min}(r^*)$. The values of $\phi_{\min}$ for different r^* are also given by Shah and Bhatti (1987).

The modeled vapor chamber for the wing leading edge heat pipe is a rectangular sector and the friction coefficient is

$$f\,\mathrm{Re}_h=24(1-1.3553\,\alpha^*+1.9467\,\alpha^{*2}-1.7012\,\alpha^{*3}+0.9564\,\alpha^{*4}-0.2537\,\alpha^{*5}) \tag{9}$$

where $\alpha^*=h/W$. The Reynolds number Re_h in Eqs. (7)–(9) is based on the hydraulic diameter D_h of the duct.

Boundary Conditions. At both ends of the heat pipe, the vapor velocity and the temperature gradients are zero:

$$z=0 \text{ and } L:\quad U=0,\ \frac{\partial T}{\partial x}=0 \tag{10}$$

In the wall and wick regions, the symmetric boundary conditions are applied except at the inner and outer shell wall surfaces and at the wick–vapor interfaces. The evaporation or condensation vapor mass flux into the vapor space, ρv, at the vapor–wick interfaces can be found from interfacial energy balances:

$$\rho v=q_{ow}/h_{fg}+q_{iw}/h_{fg}=\left[\left(k_{\mathrm{eff}}\frac{\partial T}{\partial r}\right)_{ow}-\left(k_{\mathrm{eff}}\frac{\partial T}{\partial r}\right)_{iw}\right]/h_{fg}=\begin{cases}>0 & \text{evaporation}\\ <0 & \text{condensation}\end{cases} \tag{11}$$

q_{ow}/h_{fg} and q_{iw}/h_{fg} are mass fluxes from the outer shell and inner shell wicks, respectively, and can be calculated from the temperature distributions in the outer and inner wicks. Note that Eq. (11) is also applicable to the leading edge regions, with $q_{iw}\equiv 0$.

At the condenser interfaces of the inner and outer wicks, vapor condenses and releases its latent heat energy. In order to simulate this process, two heat sources, $q_i=h_{fg}\rho_i v_i$ and $q_o=h_{fg}\rho_o v_o$, were applied at the grids next to the interfaces on the inner and outer shell wicks. Since the heat pipe shells and vapor were solved as a conjugate problem, these heat sources should be calculated from the vapor solution. In this study, the vapor was solved as a one-dimensional problem. Therefore, only the total suction mass flux ρv can be obtained by using Eq. (3) for a given vapor flow distribution in the x direction. The distribution of the total suction mass flux to the inner or outer shell wicks should be related to the radiation heat dissipative rate at the different shell surfaces, which is in turn proportional to the local radius of the individual shell for the nosecap heat pipe. By considering the relation $\rho_o v_o+\rho_i v_i=v\rho$, and $v_i\rho_i/v_o\rho_o=r_i/r_o=\gamma$, we have

$$\rho_o v_o=\rho v/(1+\gamma),\quad \rho_i v_i=\gamma\,\rho_o v_o \tag{12}$$

Note that, at the leading edge of the nosecap and wing leading edge heat pipes, $r_i=0$ and $\rho_o v_o=\rho v$. In the skirt region of the leading edge heat pipe, the heat pipe cross-sectional area is rectangular, and the radiative areas of the inner and outer shells are the same. Therefore, in Eq. (12), we can set $r_i=r_o$, which gives $\rho_o v_o=\rho_i v_i=0.5\,\rho v$.

At the outer shell wall surface, the aerodynamic heating distribution q_{local} was specified. In addition, a radiation heat flux into the ambient is superimposed at the surface. The net heat flux at the outer wall surface is

$$q_{\mathrm{net}}=q_{\mathrm{local}}-\epsilon_o\sigma(T_{os}^4-T_{am}^4) \tag{13}$$

where T_{os} and T_{am} are the outer shell wall surface and ambient temperatures. Unlike conventional heat pipes, the locations of the evaporator and condenser were not prescribed for the outer shell of the heat pipe, and may change during the transient operating period. At the inner shell wall surface, a radiation heat flux q_{is} was specified due to the radiation to the H_2 heat exchanger. Assuming the emissivity of the H_2 heat exchanger to be unity, q_{is} can be expressed as:

$$q_{is}=\epsilon_i\sigma(T_{is}^4-T_{\mathrm{sink}}^4) \tag{14}$$

where T_{is} and T_{sink} are the inner shell wall and the H_2 heat exchanger temperatures.

The conservation equations and boundary conditions in different regions were solved as a conjugate problem by applying the control-volume-based finite difference method. For more detailed information about the numerical model and procedure, the reader is referred to the paper by Cao and Faghri (1992).

Capillary and Boiling Limitations. Based on the fact that the liquid pressure drop in the circumferential direction is negligible, and the axial liquid flow resistances in the different wicks can be considered to be connected in parallel, the following relation for the capillary limit is derived:

$$\int_0^{x_{\min}}\left\{\dot{m}(s)/\left[\frac{K_oA_o}{\nu_l}+\frac{K_iA_i}{\nu_l}+\frac{K_aA_a}{\nu_l}\right]\right\}ds+\Delta p_v\le\frac{2\sigma}{r_{\mathrm{eff}}} \tag{15}$$

where K_oA_o, K_iA_i, and K_aA_a are the products of the wick permeability and the liquid flow areas for the outer shell wick, the inner shell wick, and the artery wick, respectively. r_{eff} is the effective capillary radius of the wick pores, Δp_v is the total vapor pressure drop along the heat pipe length, which can be found from the numerical solutions, and $x_{\min}$ is the location where the capillary pressure is minimum and equal to zero. In this study, $x_{\min}$ is taken to be at the condenser end cap. The total local mass flow rate $\dot{m}(s)$ is given by

$$\dot{m}(s) = \int_0^s [(v\rho)_{iw} + (v\rho)_{ow}] W d\xi \tag{16}$$

where $(v\rho)_{iw}$ and $(v\rho)_{ow}$ are the vapor mass fluxes to the vapor chamber from the inner and outer shell wicks. W is either the circumferential length of the nosecap heat pipe, or the width of the modeled section for the wing leading edge heat pipe. The relation for the boiling limit was developed by applying the theory of vapor nucleation, combined with the integrated Clausius–Clapeyron equation (Cao and Faghri, 1992):

$$\Delta T_{\text{crit}} = T_w - T_v = \frac{RT_vT_w}{h_{fg}} \times \ln\left[1 + \frac{2\sigma}{RT_v\rho_v}\left(\frac{1}{r_b} - \frac{1}{R_m}\right) + \frac{2\sigma}{RT_vr_b\rho_l}\right] \tag{17}$$

where T_w and T_v are wick–wall interface temperature and vapor space temperature, r_b is the effective radius of the vapor bubble trapped in the wick, and R_m is the radius of curvature of the liquid meniscus. If the last two terms in brackets are very small, Eq. (17) can be reduced to the commonly used relation in the literature (Chi, 1976).

Results and Discussion

The analysis of the transient and steady-state performance was first made for a nosecap heat pipe using lithium as the working fluid and a refractory metal as the container walls. The dimensions and the thermal properties of the heat pipe are: nose radius R_o = 0.04 m, adiabatic length L_a = 0.08 m, condenser length L_c = 0.7 m, vapor space height h = 0.013 m, wick and wall thickness $\delta_w = \delta_l$ = 0.6 mm, liquid artery radius R_a = 0.76 mm, skirt slope α_s = 6 deg, apex angle 2ϕ = 60 deg, heat capacity and thermal conductivity of the outer shell $(c\rho)_{os} = 2.756 \times 10^6$ J/(m^3 • K) and $(k_w)_{os}$ = 49.3 W/(m • K), heat capacity and thermal conductivity of the inner shell $(c\rho)_{is} = 3.021 \times 10^6$ J/(m^3 • K), and $(k_w)_{is}$ = 40.64 W/(m • K). The wick porosities are ω_n = 0.3 and ω_s = 0.5 at the nose and skirt regions, respectively. Figure 2 shows the normalized aerodynamic heating distribution $q_{\text{local}}/q_{\text{stagnation}}$ along the nosecap outer shell surface, which is similar to the wing leading edge ascent trajectory heating distribution. The stagnation heat flux used in the calculation is 340.5 W/cm^2 (300 Btu/s • ft^2). The numerical simulation started with an initial system temperature of 1050 K and zero initial velocity in the vapor chamber. At t = 0, the aerodynamic heating distribution was imposed at the outer shell, and the transient operation of the heat pipe began. The outer shell wall surface temperature of the nosecap heat pipe for different time periods is also shown in Fig. 2. The wall surface temperature rose gradually and reached steady state in about 400 s. The highest temperature occurred at the nosecap stagnation point where the local aerodynamic heat flux is much higher than that over the rest of the surface.

When the heat pipe reached steady state, the total heat input to the heat pipe and the total heat output should be the same, which is true for the present case. The total heat input is the integral of q_{local} over the outer shell surface, which is constant for all time. The total radiative heat output is the sum of the integrals of the radiative heat fluxes over the outer and the inner shell surfaces. Both radiative heat fluxes were dependent on the wall surface temperature. When the wall surface temperatures increased with time, the total radiative heat output increased accordingly. When the heat pipe reached steady state, the difference between the total heat input and the total radiative heat output was less than 0.5 percent. The fact that the total radiative heat output approached the total heat input at steady state also validates the present computer code.

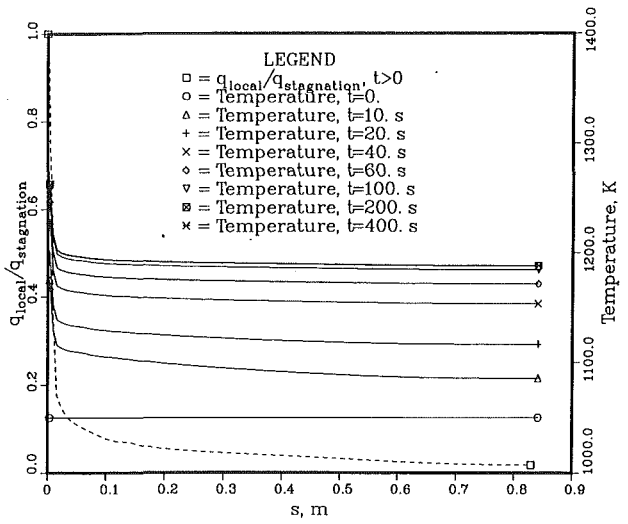

Fig. 2 Aerodynamic heating distribution and outer shell wall surface temperature for different time periods

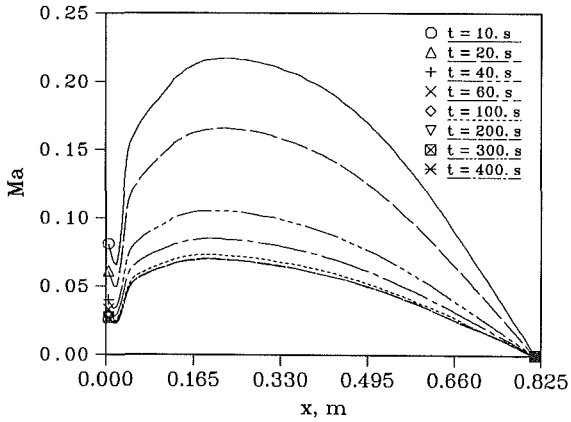

Fig. 3 Axial vapor Mach numbers along the nosecap heat pipe for different time periods

Figure 3 shows the axial vapor Mach number along the vapor chamber for different time periods. In the early time periods, the vapor velocity and Mach number were relatively high. However, they dropped sharply with time and became very small at steady state due to the much larger vapor density at a higher heat pipe working temperature. The vapor density is rather uniform along the heat pipe length. This is due to the high working temperature and the sufficiently large vapor space that provided little resistance to the vapor flow down the length of the heat pipe. As a result, the sonic limit did not occur in the steady-state operation for the present heat pipe design.

The liquid pressure in the upper shell wick was first calculated by assuming a constant permeability of $K = 2.0 \times 10^{-10}$ m^2 in the upper and lower wicks and a permeability of $K = 7.3 \times 10^{-8}$ m^2 for the axial arteries in the skirt region. The steady-state liquid pressure distribution in the axial direction (the curve labeled case 1) was plotted in Fig. 4 along with the steady-state vapor pressure distribution. The liquid pressure drop is large in the nose region due to the very high aerody-

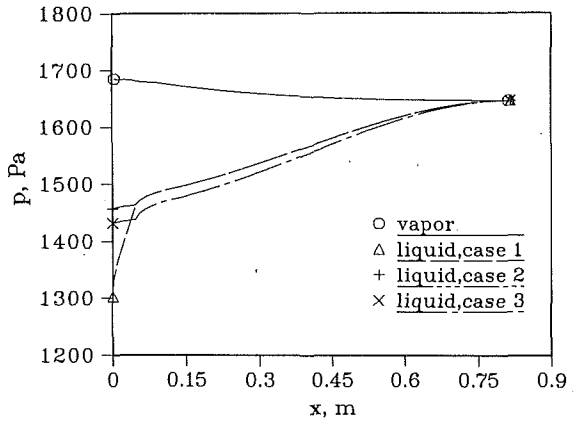

Fig. 4 Steady-state liquid and vapor pressure distributions along the outer shell of the nosecap heat pipe

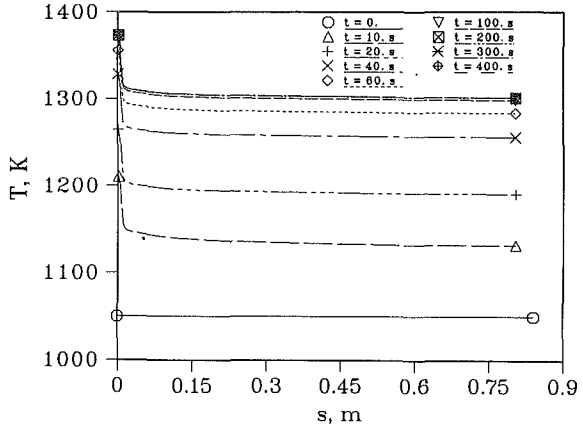

Fig. 5 Outer shell wall surface temperature of the wing leading edge heat pipe for different time periods.

namic heating near the stagnation point and small liquid flow area available in the nose region. The calculation was repeated with a much larger value of permeability, $K = 5.0 \times 10^{-9}$ m^2, in the nose region of the outer shell wick, with the other parameters being the same. The liquid pressure distribution was plotted in the same figure and labeled case 2. The pressure drop in the nose region is much smaller than that in the previous case. The curve labeled with case 3 is the liquid pressure drop with the same high permeability in the nose region of the outer shell wick, and a much smaller permeability $K = 10^{-11}$ m^2 in the skirt wicks. The liquid pressure drop is only slightly larger than that for case 2. The liquid pressure distributions for the above three cases indicate that the total liquid pressure drops are somewhat insensitive to the outer and inner shell wick structures in the skirt region due to the function of the axial arteries. However, the liquid pressure drop is very sensitive to the wick structure in the nose region due to the intense aerodynamic heating and small flow area available there. A direct measure to overcome this difficulty is to increase the wick permeability in the nose region. However, a wick structure with large permeability may not be able to offer an effective pore radius small enough to provide sufficient capillary pumping force. In this case, a special wick structure is needed over the nose region to optimize these functions. The boiling limitation was considered by applying Eq. (17). The maximum temperature drop across the wick structures for the present nosecap heat pipe is much smaller than the critical temperature drop ΔT_{crit} from Eq. (17). Therefore, the boiling limitation will not occur for the present heat pipe.

Computations were also made for the wing leading edge heat pipe shown in Fig. 1. Most of the dimensions and thermal properties used in the calculation are the same as those of the nosecap heat pipe, so only the different parameters are listed here: leading edge radius $R_o = 0.02$ m, vapor space height $h = 0.0176$ m, the heat capacity and thermal conductivity at the leading edge wall are 2.756×10^6 J/(m • K) and 49.3 W/(m • K). The heat capacity and thermal conductivity at skirt walls are 3.02×10^6 J/(m • K) and 40.64 W/(m • K). The heat capacity and thermal conductivity for the wick are 2.63×10^6 J/(m • K) and 66.05 W/(m • K), and the porosity in the wick is $\omega = 0.4$. The aerodynamic heating conditions and the wick structures are also the same as those for the nosecap heat pipe. Figure 5 shows the outer shell wall temperature for different time periods. The general trends are similar to those of the nosecap heat pipe except that the steady-state wall temperature and vapor pressure are relatively higher than those of the nosecap heat pipe. Compared to the nosecap heat pipe with almost the same axial dimension, the radiation area available per unit heat input for the leading edge heat pipe is smaller than that of the nosecap heat pipe, and the working temperature is correspondingly higher. Also, the vapor space for this leading edge heat pipe design is larger than that of the nosecap heat pipe, and as a result, the maximum vapor Mach number is relatively smaller. In summary, the numerical model presented in this paper provided a generalized method to analyze the transient and steady-state performance of nosecap and wing leading edge heat pipes.

References

Camarda, C. J., 1988, "Thermostructural Applications of Heat Pipes for High-Speed Aerospace Vehicles," *Proc. Third Int. Heat Pipe Conf.*, Tsukuba, Japan, pp. 31–43.

Cao, Y., and Faghri, A., 1990, "A Transient Two-Dimensional Compressible Analysis for High Temperature Heat Pipes With a Pulsed Heat Input," *Numer. Heat Transfer*, Part A, Vol. 18, pp. 483–502.

Cao, Y., and Faghri, A., 1991, "Transient Multidimensional Analysis of Nonconventional Heat Pipes With Uniform and Nonuniform Heat Distributions," ASME JOURNAL OF HEAT TRANSFER, Vol. 113, pp. 995–1002.

Cao, Y., and Faghri, A., 1992, "Analyses of Transient and Steady-State Performances of Nosecap and Wing Leading Edge Heat Pipes," *Proc. ASME Winter Annual Meeting*, Anaheim, CA, ASME HTD-Vol. 221, pp. 43–52.

Chi, S. W., 1976, *Heat Pipe Theory and Practice*, Hemisphere Publishing Corp., Washington, DC.

Faghri, A., Buchko, M., and Cao, Y., 1991, "A Study of High Temperature Heat Pipes With Multiple Heat Sources and Sinks: Part II—Analysis of Continuum Transient and Steady State Experimental Data With Numerical Predictions," ASME JOURNAL OF HEAT TRANSFER, Vol. 113, pp. 1010–1016.

Shah, R. K., and Bhatti, M. S., 1987, "Laminar Convective Heat Transfer in Ducts," in: *Handbook of Single Phase Convective Heat Transfer*, S. Kakac et al., eds., Wiley, New York.